PAPER

High spatial resolution direct conversion amorphous selenium X-ray detectors with monolithically integrated CMOS readout

JINST

PUBLISHED BY IOP PUBLISHING FOR SISSA MEDIALAB

RECEIVED: *February 13, 2023*
ACCEPTED: *March 20, 2023*
PUBLISHED: *April 13, 2023*

High spatial resolution direct conversion amorphous selenium X-ray detectors with monolithically integrated CMOS readout

Z. Han,[a] A. Mukherjee,[a] A. Albert,[b] A.K. Rumaiz,[c,*] I. Harding,[d] M.W. Tate,[e] S.M. Gruner,[e] J. Thom-Levy,[b] A.J. Kuczewski,[c] D.P. Siddons,[c] G.A. Carini,[d] J. Stavro,[f] S. Léveillé,[g] D. Vasileska,[h] W. Zhao[f] and A. Goldan[i]

[a] *Department of Electrical and Computer Engineering, Stony Brook University, Stony Brook, NY 11794, U.S.A.*
[b] *Laboratory for Elementary-Particle Physics, Cornell University, Ithaca, NY 14853, U.S.A.*
[c] *NSLS II, Brookhaven National Laboratory, Upton, NY 11973, U.S.A.*
[d] *Instrumentation Division, Brookhaven National Laboratory, Upton, NY 11973, U.S.A.*
[e] *Laboratory of Atomic and Solid State Physics, Cornell University, Ithaca, NY 14853, U.S.A.*
[f] *Department of Radiology, School of Medicine, Stony Brook University, Stony Brook, NY 11794, U.S.A.*
[g] *Analogic Corporation, Montreal, QC H4R 2P1, Canada*
[h] *School of Electrical, Computer and Energy Engineering, Arizona State University, Tempe, AZ 85281, U.S.A.*
[i] *Department of Radiology, Weill Cornell Medical College, Cornell University, New York, NY 10021, U.S.A.*

E-mail: rumaiz@bnl.gov

ABSTRACT: Recent progress in the field of micron-scale spatial resolution direct conversion X-ray detectors for high-energy synchrotron light sources serve applications ranging from nondestructive and noninvasive microscopy techniques which provide insight into the structure and morphology of crystals, to medical diagnostic measurement devices. Amorphous selenium (a-Se) as a wide-bandgap thermally evaporated photoconductor exhibits ultra-low thermal generation rates for dark carriers and has been extensively used in X-ray medical imaging. Being an amorphous material, it can further be deposited over large areas at room temperatures and at substantially lower costs as

*Corresponding author.

https://doi.org/10.1088/1748-0221/18/04/P04021

2023 JINST 18 P04021

compared to crystalline semiconductors. To address the demands for a high-energy and high spatial resolution X-ray detector for synchrotron light source applications, we have thermally evaporated *a*-Se on a Mixed-Mode Pixel Array Detector (MM-PAD) Application Specific Integrated Circuit (ASIC). The ASIC format consists of 128×128 square pixels each 150 µm on a side. A 200 µm *a*-Se layer was directly deposited on the ASIC followed by a metal top electrode. The completed detector assembly was tested with 45 kV Ag and 23 kV Cu X-ray tube sources. The detector fabrication, performances, Modulation Transfer Function (MTF) measurements, and simulations are reported.

KEYWORDS: Materials for solid-state detectors; Radiation-hard detectors; Solid state detectors; X-ray detectors

2023 JINST 18 P04021

Contents

1 Introduction

Hard X-ray/Gamma Ray detection is currently achieved with semiconductor detectors that have several limitations. For example, silicon — an extremely mature technology — is essentially transparent to high energy photons for typical sensor thickness (rarely thicker than 1 mm), germanium-based detectors require cryogenic cooling, while Cadmium Zinc Telluride (CZT)-based detectors are hampered by the difficulty and cost of producing suitably large crystals. Furthermore, conventional high-Z crystals such as Ge and CZT have limited spatial resolution (125 microns [1] in case of a 3 mm thick Ge). Scintillator crystals coupled to photodetectors make use of secondary detection, which is sub-optimal since it causes a broadening of the spectroscopic lines [2]; in addition, photodetectors are prone to radiation damage. Solid-state amorphous selenium (a-Se) sensors have achieved considerable commercial success in X-ray imaging including mammography and general radiography, as a-Se is a large area, wide band-gap, room-temperature semiconductor that has very low thermal noise, and a wide detectable wavelength ranging from visible light [3, 4], to X-rays [5, 6]. It has a low melting point and high vapor pressure making it easy to deposit uniform layers over a large area by thermal evaporation. This contrasts with many crystalline semiconductors, where making large detector grade wafers remains challenging. a-Se has been used up to now mainly in medical applications [7, 8] and in cameras for visible light applications [9, 10]. In addition to ease of fabrication, a-Se detector is expected to have a high spatial resolution (below 10 microns) which can support the development of smaller readout pixels.

2023 JINST 18 P04021

Current state-of-the-art commercial a-Se medical imaging detectors typically utilize thin-film transistor (TFT) arrays [11]. However, complementary metal-oxide-semiconductor (CMOS) arrays allow for much smaller pixel size as well as the possibility of doing charge integration and photon counting. As mentioned before, the deposition temperatures for a-Se are low enough that it may be deposited directly on top of a CMOS readout application-specific integrated circuit (ASIC) without damage to the circuitry. While a-Se coupled with CMOS ASICs have been fabricated before [12], a-Se has not been adequately studied for high-flux applications. To determine the viability of such a detector, a-Se was deposited directly on a Mixed-Mode Pixel Array Detector (MM-PAD) CMOS ASIC [13] and a series of diagnostic and characterization tests were performed. In the past, the MM-PAD ASIC has been successfully used as a photodetector with Si and CdTe [14].

In this paper, we first introduce the MM-PAD CMOS readout, then we detail the detector fabrication, and analyze its performance. We have performed detailed modulation transfer function (MTF) measurements of a-Se detector for different excitation energies. The hole transport was modeled using the Monte Carlo-Boltzman transport equation and a simulation for intrinsic spatial resolution of a-Se was made.

2 Detector overview

2.1 ASIC

The MM-PAD was utilized as an ASIC readout in this X-ray detector. The details of the readout chip can be found elsewhere [13, 15]. Briefly, charge integrating amplifier accumulates the signal generated in the sensor diode onto a small (50 fF) capacitor. The small feedback capacitance is chosen to provide single photon sensitivity at low intensity levels. The output of the amplifier is monitored by a comparator during integration. When a preset threshold is exceeded during exposure, logic increments a counter and initiates an event that removes a fixed amount of charge from the integrating feedback capacitor. This mechanism keeps the integrator within the operating range and increases the dynamic range. Integration continues during the charge removal thereby incurring no dead time. Pixel output at the end of a frame is mixed mode, consisting of an analog value that is sampled from the front-end integrator and the 18 bit digital word that tracks the number of charge removal events. The analog value is digitized with a 12 bit analog-to-digital converter (ADC) located external to the chip, running at 2 MHz.

2.2 Detector fabrication

Each pixel in the bare MM-PAD ASIC has an aluminum pad that is intended as the base for a solder bump to connect to pixelated sensor, as shown in figure 1. These pads cover only a small fraction of the pixel area. In order to increase the fill factor of the surface onto which the a-Se would be deposited, the Al bumps were extended to cover most of the pixel. The Al metal extension was defined on the ASIC using a commercial laser writer and the metal patterned with a standard lift-off process, so that the entire pixel surface was covered, save for a gap of 20 µm between adjacent pixels. Following the pad extension, a 200 µm thick a-Se layer was thermally deposited over most of the 128×128 pixel area of the MM-PAD via a shadow mask. A Chromium (Cr) top electrode was subsequently deposited via the same shadow mask. The top electrode was connected to a bias wire with conductive silver epoxy and finally the sensor assembly was capped with parylene.

2023 JINST 18 P04021

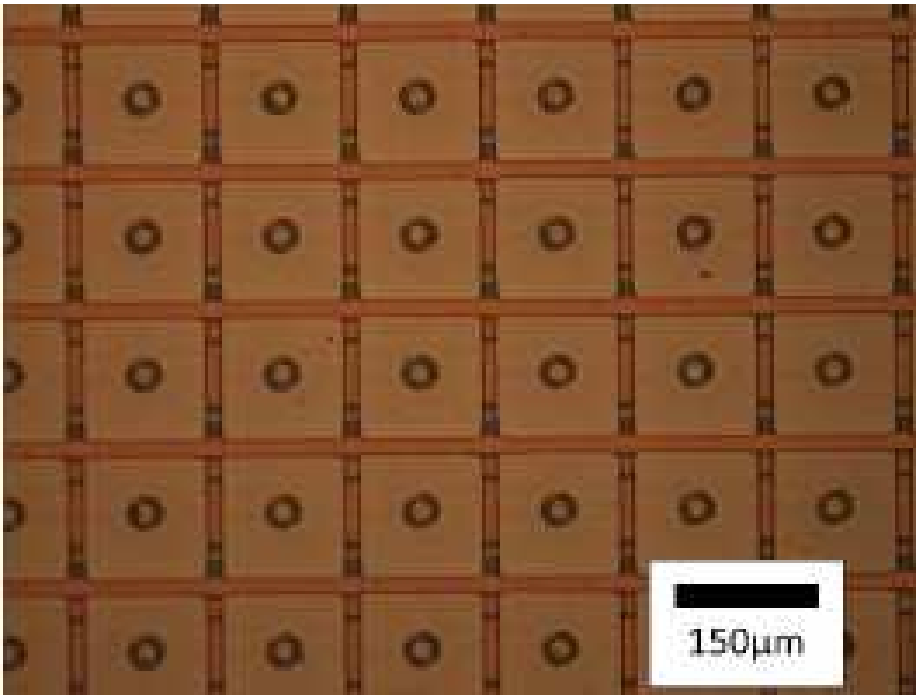

Figure 1. MM-PAD with readout pads extends. The width of the extended pads is 130 µm.

2.3 Test system setup

A full-scale MM-PAD has 2X3 tiled modules with a single tile consisting of 128X128 pixels. For the measurement reported in this work, we used a single 128X128 pixel ASIC with *a*-Se thermally evaporated on it. The ASIC with the *a*-Se was then mounted to an Aluminium heat sink using thermal conductive epoxy and then wire-bonded to the printed circuit board (PCB). The curing of the epoxy was done at room temperature to avoid the crystallization of selenium. All measurements were performed at room temperature with a bias set at 10 V/µm. The PCB is mated with a secondary long circuit board that is used for routing electric signals to and from the detector module. A dedicated FPGA is used to assemble and organize the data stream, which is then sent via a Cameralink connection to a PC for storage and analysis. X-ray response was performed with a 45 kV Ag tube. Supporting equipment includes tungsten edge, filters, attenuators, etc. The complete test setup is shown in figure 2(a) and figure 2(b).

3 Detector characterization

3.1 Radiographs

A flood illumination of a 45 kV X-ray Ag tube with a 1 mm Al filter is shown in figure 3(a). The image shown is an average of 100 frames each with 100 ms exposure time. The flood illumination shows a uniform response with 1.6% r.m.s. on the flat field. The dark feature on the upper right is the X-ray shadow of the HV bias wire and the securing spot of silver epoxy. Figure 3(b) shows a high-contrast image of a bulb without flat field correction. To measure the noise of the detector, we acquired 100 images with no X-ray signal. We measured 883 e-r.m.s. noise for the *a*-Se detector

2023 JINST 18 P04021

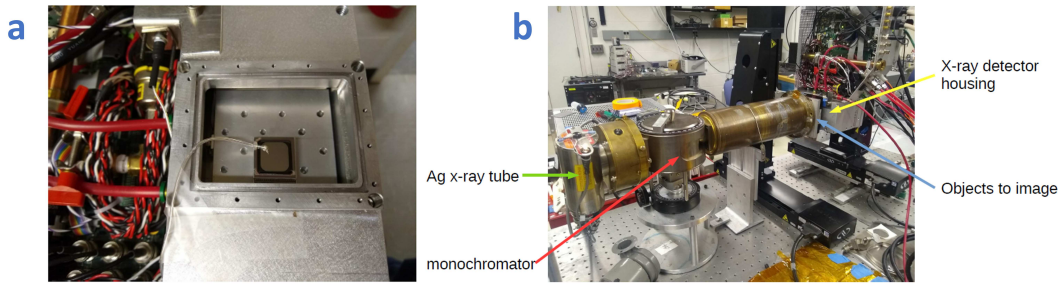

Figure 2. Test setup for the detector. (a) the front figure of the detector. The wire extending off to the left is the HV bias wire that is bonded to the top Cr electrode with conductive epoxy. (b) The figure of the whole test system including Ag X-ray tube, monochromator, and objects for imaging.

(compared with 361 e-r.m.s. for Silicon). The observed noise is independent of bias voltage. We also observed similar noise in the edge pixels which were not deposited with a-Se. This indicates that the increase in noise is mainly due to the increase in pixel capacitance. The measured dark current was 4 fA/pixel.

To measure charge collection, a series of signals were acquired when the detector was illuminated with a small X-ray spot from a monochromator (Ag Kα 22.1 keV). The flux measured with Amptek CdTe detector was found to be 2.4×10^4 X-rays/s. The integrated response from the small spot illumination was recorded as a function of bias voltage. The measured pixel current in ADU was calibrated using a single X-ray response measured with a silicon sensor. Figure 4 shows the charge collected versus sensor bias voltage. The plot shows a fairly linear relationship with no saturation observed.

3.2 Dynamic response

The dynamic response of a photodetector is an important factor that determines its performance in terms of its ability to accurately and reliably detect X-ray signals over a range of intensities and timescales. The dynamic response of a photodetector is influenced by various factors, such as its responsivity, and recovery time, and can have significant impacts on the accuracy and precision of the measured signals. The detector's dynamic response was tested by opening and closing the shutter. A flood X-ray illumination with a knife edge was irradiated to the detector first then the shutter was turned off in front of the detector. The detector's response variations were recorded. The normalized intensity was calculated by taking an average of pixels in the illuminated area. Figure 5 shows the normalized signal response. The intensity of the signal exhibits a rapid initial drop after the exposure period ends, but there is still a long, tailing decay over several seconds. The long signal decay is mainly attributed to the detrapping of charges in shallow traps [16]. While it is also known that charge injection from the positive bias electrode due to an increase in the electric field because of electrons trapped in the bulk can also lead to a slow signal response, appropriate blocking contacts can minimize this effect. Figure 6 shows the decay of the detector's response with time beginning with 100 ms before the shutter closes until 2400 ms after the shutter closes.

2023 JINST 18 P04021

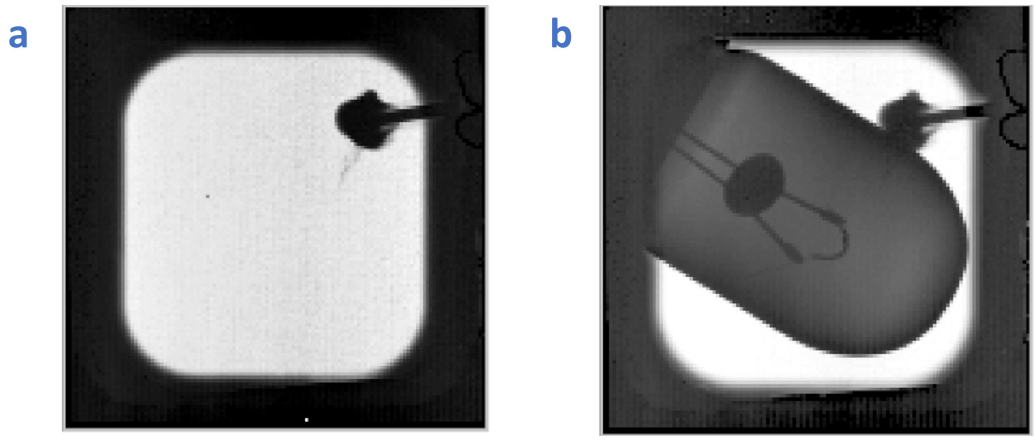

Figure 3. The image result of the detector. (a) Image of a flood illumination under 45 kV X-ray tube. The white area shows the detector area and the top right is the shadow of silver paste. (b) A bulb was positioned in front of the detector and the detector was illuminated by Ag 45 kV X-rays. The resulting image of the bulb was clearly captured by the detector.

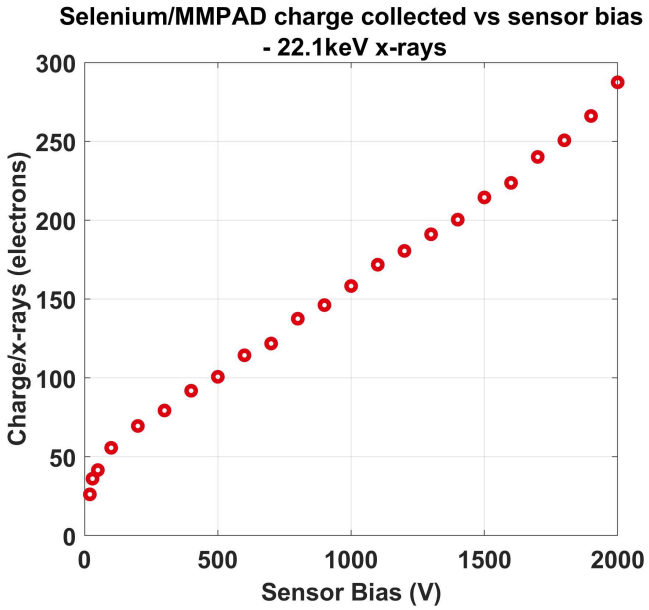

Figure 4. The relationship between the charge collected and the sensor bias is fairly linear, with no evidence of saturation observed up to 2000 V. A mean of 288 e- are collected from each 22.1 keV X-ray with a bias of 2000 V.

2023 JINST 18 P04021

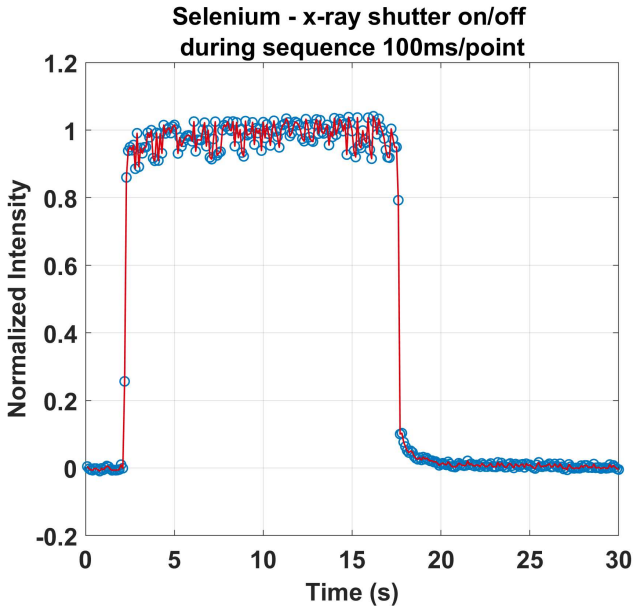

Figure 5. Detector's dynamic response during the shutter open and close. The response dropped rapidly after the shutter closed. A tail is observed prior to the response intensity falling to zero.

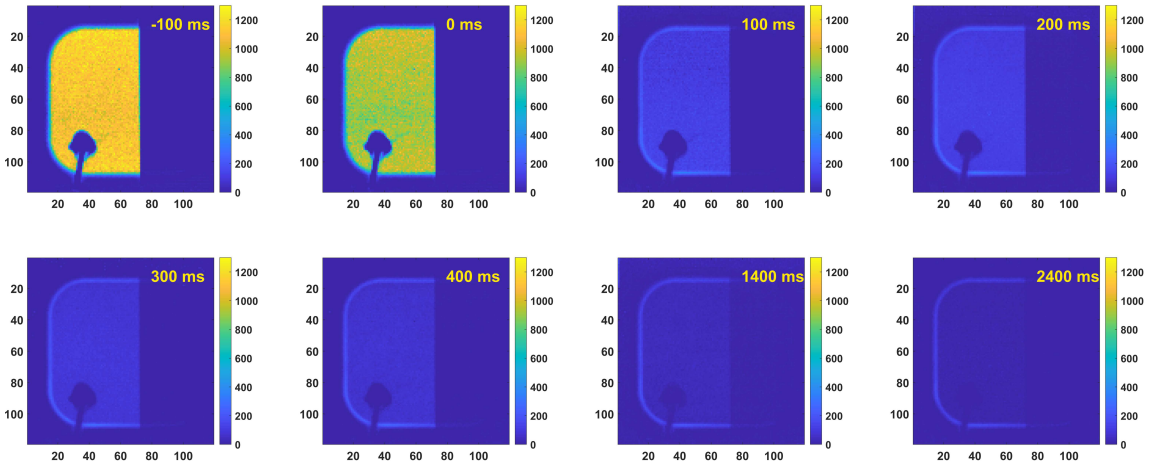

Figure 6. These figures depict the extinction lag in the *a*-Se response via successive detector frames as the shutter transitions from the on to the off state, with the response being recorded from 100 ms prior to the shutter closure until 2400 ms after the shutter closure.

3.3 Spatial resolution

3.3.1 Experimental results

The spatial resolution of the detector can be obtained by measuring the detector response to a step function of X-ray intensity vs. position, commonly referred to as the edge spread function (ESF). The ESF gives a direct measure of charge cloud size in the detector and is a metric for evaluating the spatial resolution of the detector. The ESF can be measured by placing a tantalum knife edge at

2023 JINST 18 P04021

some small angle with respect to the detector. At such a small tilt, the ESF can be sampled at sub-pixel resolution in a single image as pixels along the knife edge are covered fractionally more and more by the knife as one translates along the knife edge. Figure 7 shows the radiograph of the knife edge illuminated by Ag anode (22.1 kV). The knife-edge data is normalized by dividing by a data set taken without the knife. The measurements were then repeated for different X-ray energies to obtain the dependence of spatial resolution (on X-ray energies). The response intensity data within 2-pixel proximity to the edge for two different X-ray energies (8.98 KeV, Cu anode, and 22.1 KeV Ag anode) are shown in figure 8(a), 8(b). The energy of the excitation X-ray was measured with a CdTe drift detector is shown in figure 8(c), 8(d). The ideal knife-edge response would be a linear ramp across one pixel. Charge diffusion leads to a deviation from an ideal response. The convolution of the ideal response ramp (red line in figure 8(a), 8(b)) with a Gaussian with varying width was fit to the ESF data. The width of the fitted Gaussian is a measure of the charge spread in the sensor. The fitted function had a width of 5.12, and 10.1 µm for X-ray energies 8.98, and 22.1 KeV respectively. It is possible to obtain the line spread function (LSF) by taking the derivative of the fit to ESF. The Fourier transform of the LSF is used to determine the modulation transfer function (MTF). The full width at half maximum (FWHM) of the Gaussian function used in figure 8(a), 8(b), was used to calculate the MTF as shown in figure 8(e), 8(f). Setting a threshold of 10% for the MTF, the spatial frequency limitation for imaging has also been shown in figure 8(e), 8(f).

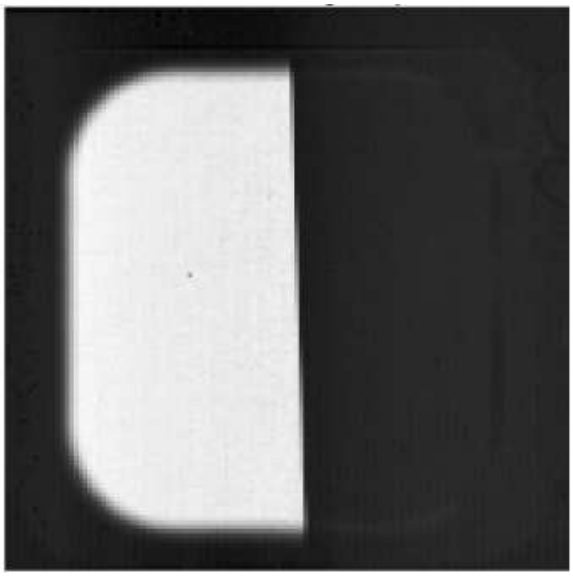

Figure 7. The real image of knife edge response. The left white side was the detector area shined under the X-ray and the right dark side was the area covered by the tantalum knife.

3.3.2 Monte Carlo simulation results

An inherent limitation to spatial resolution is the blur caused by the hole drifting process in *a*-Se, which has been modeled below. This inherent spatial blur occurs due to drifting holes under the influence of an electric field, interrupted by phonon, hole-dipole, and disorder scattering events, and represents the lower limit of the spatial resolution in the absence of any X-ray interactions.

2023 JINST 18 P04021

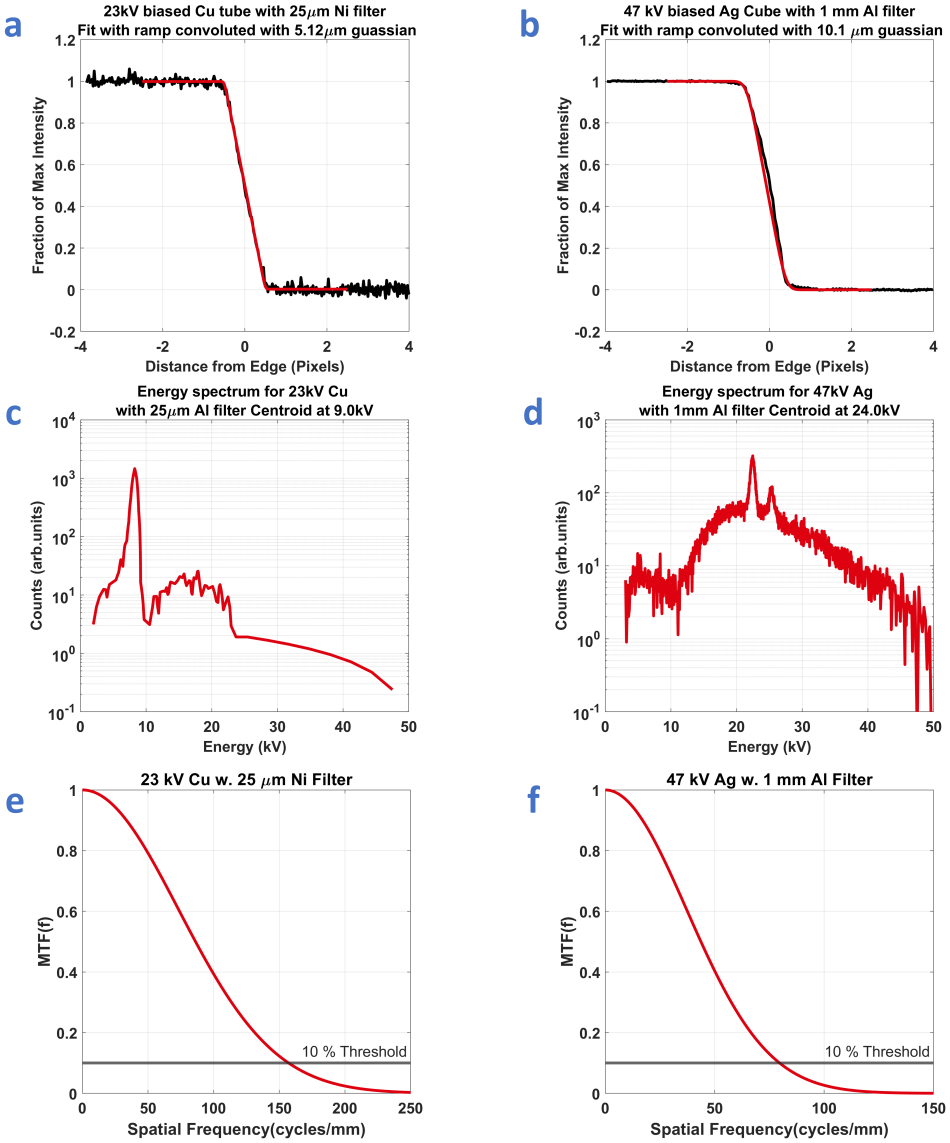

Figure 8. Top row presents the edge response signal intensity under different energy X-ray illumination. The middle row shows the corresponding energy for each X-ray illumination at (c) 23 kV Cu tube bias with 25 µm Ni filter, and (d) 47 kV Ag tube bias with 1 mm Al filter. The bottom plots (e) and (f) show the MTF calculated from the FWHM of the Gaussian used to convolve the ESF.

The hole transport in *a*-Se was simulated using an in-house Monte Carlo-Boltzmann Transport Equation (MC-BTE) solver. Using quantum mechanical formulations based on Fermi's golden rule, we calculate the energy depended phonon scattering (acoustic, polar emission/absorption and non-polar emission/absorption), hole-dipole, and disorder scattering (caused by valence alternate pair type defects as scattering centers) rates in *a*-Se. To validate our transport model, we compare our high-field time-of-flight mobility, impact ionization gain, ensemble energy and velocity with experimental findings [17–20]. The non-ballistic nature of hole transport in *a*-Se is a result of the frequent acceleration and deceleration caused by the cumulative affect of the electric field and lattice/impurity/disorder scattering, which leads to an increased spread of holes in the direction

2023 JINST 18 P04021

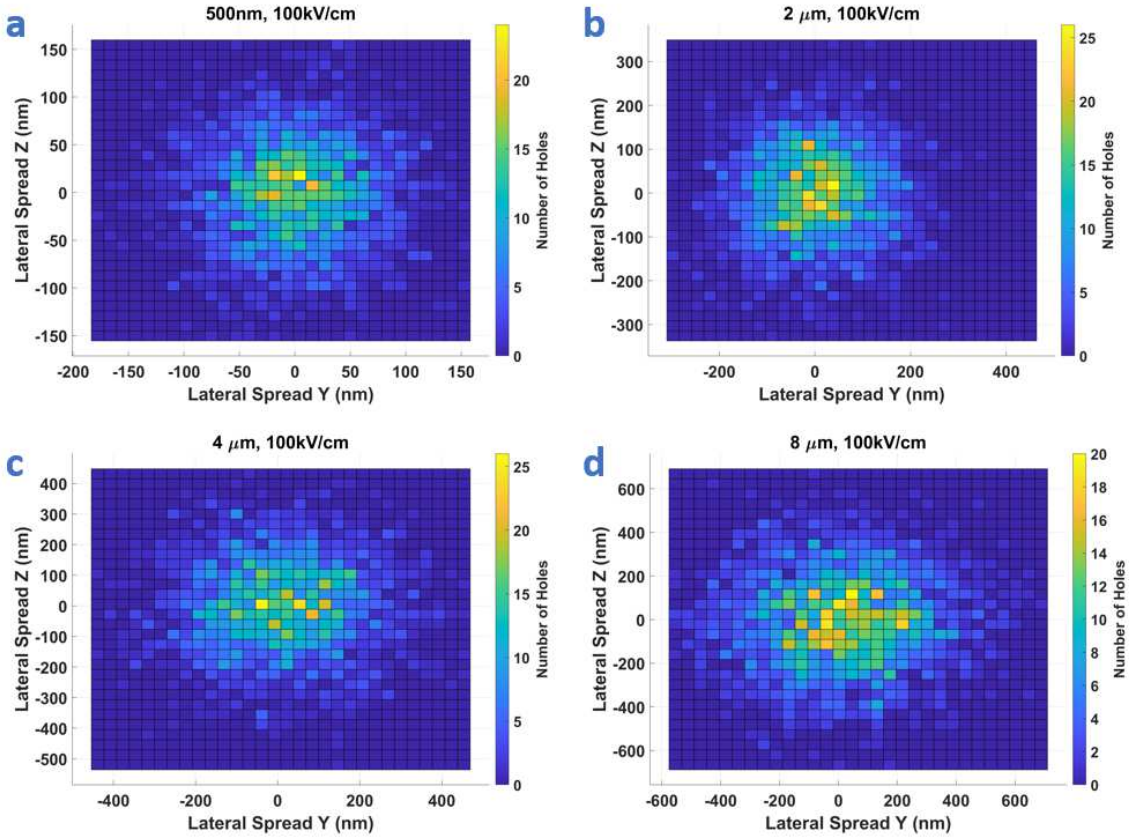

Figure 9. Monte Carlo simulation results showing the increase in the spatial spread of the charge cloud of 2000 holes injected at $x = 0$. The lateral spread as a function of the electric field at the end of (a) 500 nm, (b) 2 µm, (c) 4 µm and (d) 8 µm of travel in a-Se is simulated at 10 V/µm. The electric field is applied along the x-axis in the simulation.

lateral to the applied electric field. Here, we model this low-field (10 V/µm) spatial resolution in a-Se thin-films.

A metric measured in the spatial domain that describes the spatial resolution of an imaging system is the point spread function (PSF). The PSF is a two-dimensional (2D) function and is the most basic measure of the resolution properties of an imaging system. A point source is an input to the imaging system, and the PSF is the impulse response of the imaging system to that point input. In the MC simulation, 2000 hole carriers were injected into the device at coordinates $(0, 0, 0)$ and the simulation was run until all carriers were collected after a drift length of 500 nm, 2 µm, 4 µm and 8 µm at an electric field of 10 V/µm as shown in figure 9(a)–9(d).

The FWHM for the charge cloud spread at the simulated drift length was calculated by fitting the results in figure 9 to a Gaussian distribution in the Y-axis and Z-axis lateral spread directions. The FWHM calculated as a function of the drift length is shown in figure 10. A polynomial fit proportional to the square root of the drift length was used to fit the simulated FWHM for 500 nm, 2 µm, 4 µm, and 8 µm a-Se drift lengths, as shown by the solid line in figure 10. This fit predicts a FWHM spatial blur of 2.4 µm, corresponding to a drift length of 200 µm at 10 V/µm. Next, the MTF was obtained in the 2 lateral directions to the applied electric field, as shown in figure 11. The

2023 JINST 18 P04021

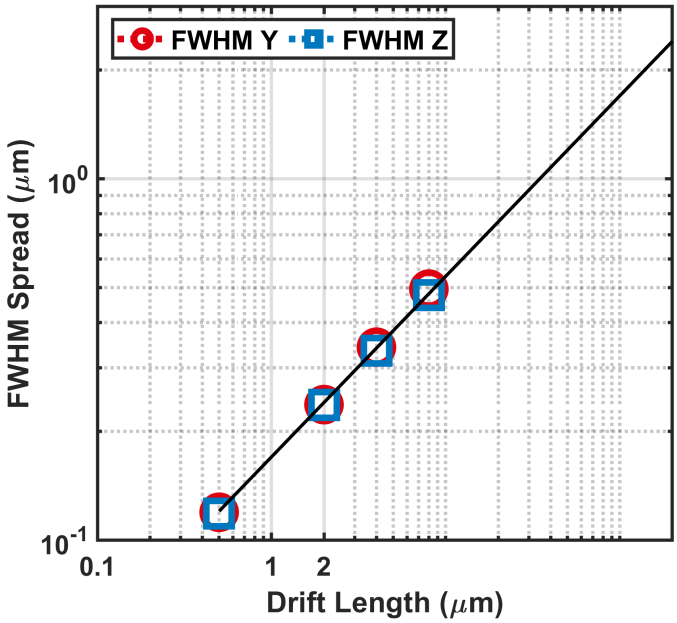

Figure 10. The FWHM simulated for a-Se drift lengths of 500 nm, 2 µm, 4 µm and 8 µm. The MC simulations predicts a FWHM of ~ 2.4 µm for a-Se drift lengths of 200 µm.

FWHM prediction for a a-Se drift length of 200 µm from figure 10 was used to predict the MTF for 200 µm a-Se drift lengths in figure 11(e).

3.3.3 Simulation methods

The line spread function was calculated along each axis by fitting a Gaussian to the PSF histogram in Matlab. The Gaussian approximation for the LSF along the lateral directions y and z is given by:

$$\mathrm{LSF}(y) = \frac{1}{\sigma\sqrt{2\pi}} e^{\frac{-y^2}{2\sigma^2}}, \tag{3.1}$$

where σ is the standard deviation of the Gaussian distribution. The MTF(f) is obtained from the Fourier transformation of the LSF:

$$\mathrm{MTF}(f) = \frac{1}{\sqrt{2\pi\sigma^2}} \int_{-\infty}^{\infty} e^{\frac{-y^2}{2\sigma^2}} e^{2\pi i f y} \mathrm{d}y, \tag{3.2}$$

$$\mathrm{MTF}(f) = \frac{1}{\sqrt{2\pi\sigma^2}} \left[\int_{-\infty}^{\infty} e^{-\frac{1}{2\sigma^2}(y - 2\pi i \sigma^2 f)^2} \mathrm{d}y \right] e^{\frac{1}{2\sigma^2}(2\pi i \sigma^2 f)^2}, \tag{3.3}$$

the Fourier transformation is evaluated to be:

$$\mathrm{MTF}(f) = e^{2\pi^2\sigma^2 f^2}. \tag{3.4}$$

4 Conclusion

A new X-ray detector consisting of a-Se and MM-PAD CMOS readout is fabricated. Characterization measurements were conducted for this detector. The performance of the a-Se detector shows

2023 JINST 18 P04021

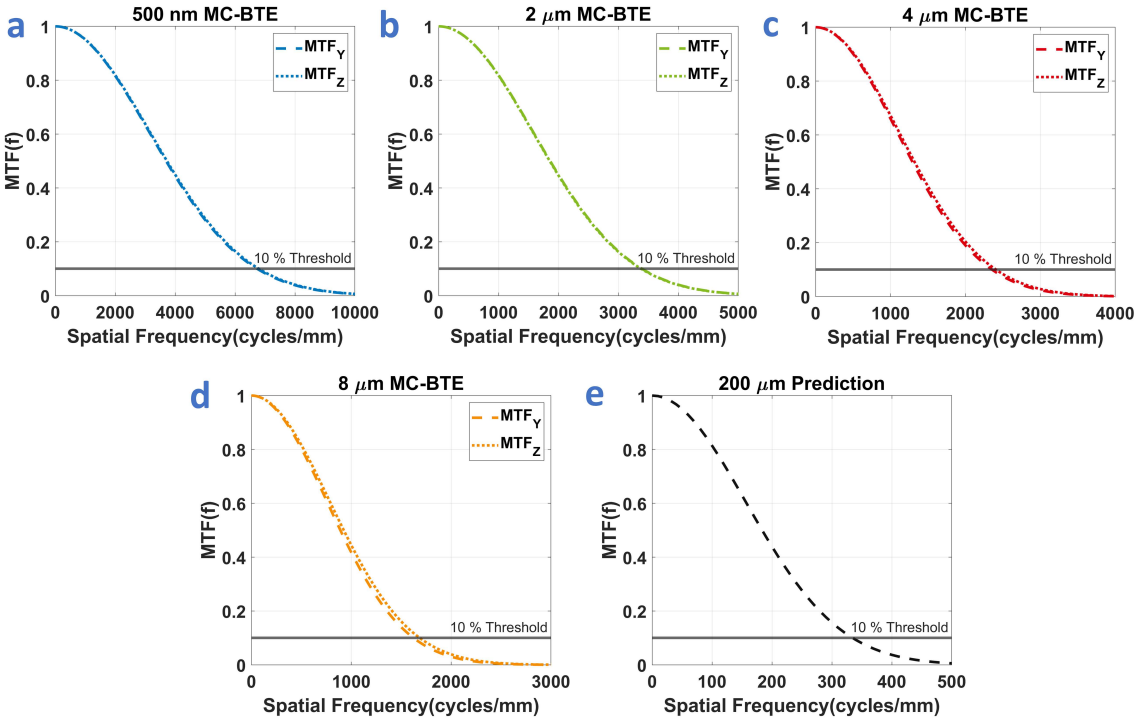

Figure 11. The simulated MTF as a function of spatial frequency at the end of (a) 500 nm, (b) 2 µm, (c) 4 µm and (d) 8 µm of travel in *a*-Se at 10 V/µm. The electric field is applied along the x-axis. (e) The predicted MTF for 200 µm *a*-Se drift length.

a high spatial resolution. However, the dynamic response shows signal decay over seconds. While this characteristic of the detector makes it less suitable for time-resolved measurements, the high spatial resolution obtained by the detector at high-energies makes it a useful tool in cases where the time resolution is set by the X-ray duration, such as single-shot radiography. The macroscopic details of hole transport in *a*-Se was simulated by using an in-house MC-BTE technique in which the carrier free-flights are interrupted by scattering from acoustic, polar, and non-polar optical phonons, disorder, and dipole scattering interactions to investigate the intrinsic spatial resolution floor in the absence of any X-ray interaction. The MC simulations predict an FWHM of 2.4 µm for *a*-Se drift lengths of 200 µm, which is lower than the experimentally measured value at about 5 µm (for Cu anode). The MC simulations sets the lower limit for the FWHM while ignoring the contributions from Coulombic repulsion, depth of interactions etc.

Acknowledgments

Support for detector development at Cornell has come from U.S. Department of Energy grants DEFG02-10ER46693, DE-SC0016035, DE-SC0004079, and DE-SC0017631. Support for work at Stony Brook University has come from the National Institutes of Health (No. R01EB026644). The author D.V. acknowledges the financial support from the National Science Foundation (ECCS-2025490 and ECCS-2048400). We would like to acknowledge Antonio Verderosa, Don Pinelli, and Joseph Pinz from the High Density Interconnect Laboratory at Brookhaven National Laboratory for help with mounting and wire-bonding the detector.

2023 JINST 18 P04021

References

[1] A.K. Rumaiz et al., *Multi-element Germanium Detectors for Synchrotron Applications*, 2018 *JINST* **13** C04030 [arXiv:1804.08660].

[2] C.M. Castelli, N.M. Allinson, K.J. Moon and D.L. Watson, *High spatial resolution scintillator screens coupled to CCD detectors for X-ray imaging applications*, *Nucl. Instrum. Meth. A* **348** (1994) 649.

[3] H. Kannan et al., *Ultralow dark currents in avalanche amorphous selenium photodetectors using solution-processed quantum dot blocking layer*, *ACS Photonics* **7** (2020) 1367.

[4] A. Mukherjee et al., *Vertical Architecture Solution-Processed Quantum Dot Photodetectors with Amorphous Selenium Hole Transport Layer*, *ACS Photonics* **10** (2023) 134.

[5] A. LaBella, W. Zhao and A.H. Goldan, *Multi-Well Avalanche Selenium Detector for Time-of-Flight PET*, in proceedings of the *2019 IEEE Nuclear Science Symposium and Medical Imaging Conference (NSS/MIC)*, Manchester, U.K., 26 October–2 November 2019, IEEE (2019), pp. 1–4 [DOI:10.1109/nss/mic42101.2019.9059675].

[6] J.R. Scheuermann, A. Howansky, M. Hansroul, S. Léveillé, K. Tanioka and W. Zhao, *Toward scintillator high-gain avalanche rushing photoconductor active matrix flat panel imager (SHARP-AMFPI): initial fabrication and characterization*, *Med. Phys.* **45** (2018) 794.

[7] S. Kasap et al., *Amorphous and polycrystalline photoconductors for direct conversion flat panel X-ray image sensors*, *Sensors* **11** (2011) 5112.

[8] D.L.Y. Lee, L.K. Cheung, B.G. Rodricks and G.F. Powell, *Improved imaging performance of a* $14'' \times 17''$ *direct radiography system using a Se/TFT detector*, in *Medical Imaging 1998: Physics of Medical Imaging*, proceedings of the *Medical Imaging '98* San Diego, CA, U.S.A., 21–26 February 1998, J.T. Dobbins III and J.M. Boone eds., SPIE (1998), pp. 14–23 [*Proc. SPIE* **3336** (1998) 14].

[9] K. Tanioka, K. Shidara and T. Harai, *Highly sensitive camera tube using avalanche multiplication in an amorphous selenium photoconductive target*, in *High-Resolution Sensors and Hybrid Systems*, proceedings of the *SPIE/IS&T 1992 Symposium on Electronic Imaging: Science and Technology*, San Jose, CA, U.S.A., 9–14 February 1992, M.M. Blouke, W. Chang, L.J. Thorpe and R.P. Khosla eds., SPIE (1992), pp. 2–12 [*Proc. SPIE* **1656** (1992) 2].

[10] F. Okano, J. Kumada and K. Tanioka, *The HARP High-Sensitivity Handheld HDTV Camera*, *SMPTE J.* **99** (1990) 612.

[11] W. Zhao and J.A. Rowlands, *X-ray imaging using amorphous selenium: Feasibility of a flat panel self-scanned detector for digital radiology*, *Med. Phys.* **22** (1995) 1595.

[12] C.C. Scott et al., *High-energy micrometre-scale pixel direct conversion X-ray detector*, *J. Synchrotron Radiat.* **28** (2021) 1081.

[13] M.W. Tate et al., *A medium-format, mixed-mode pixel array detector for kilohertz X-ray imaging*, *J. Phys. Conf. Ser.* **425** (2013) 062004.

[14] D. Gadkari et al., *Characterization of* 128×128 *MM-PAD-2.1 ASIC: a fast framing hard x-ray detector with high dynamic range*, 2022 *JINST* **17** P03003 [arXiv:2112.00146].

[15] H.T. Philipp et al., *High dynamic range CdTe mixed-mode pixel array detector (MM-PAD) for kilohertz imaging of hard x-rays*, 2020 *JINST* **15** P06025 [arXiv:2004.03421].

[16] B. Zhao and W. Zhao, *Imaging performance of an amorphous selenium digital mammography detector in a breast tomosynthesis system*, *Med. Phys.* **35** (2008) 1978.

2023 JINST 18 P04021

[17] A. Mukherjee, D. Vasileska, J. Akis and A.H. Goldan, *Monte Carlo solution of high electric field hole transport processes in avalanche amorphous selenium*, *ACS Omega* **6** (2021) 4574.

[18] A. Mukherjee, R. Akis, D. Vasileska and A.H. Goldan, *A Monte Carlo solution to hole transport processes in avalanche selenium semiconductors*, in *Physics and Simulation of Optoelectronic Devices XXVIII*, proceedings of the *SPIE OPTO*, San Francisco, CA, U.S.A., 1–6 February 2020, SPIE (2020), pp. 106–115 [*Proc. SPIE* **11274** (2020) 112740U].

[19] A. Mukherjee, R. Akis, D. Vasileska and A.H. Goldan, *Multiscale Modeling of High Field Hole Transport and Excess Noise in Avalanche Amorphous Selenium Layers*, in proceedings of the *2020 IEEE Nuclear Science Symposium and Medical Imaging Conference (NSS/MIC)*, Boston, MA, U.S.A., 31 October–7 November 2020, IEEE (2020), pp. 1–3.

[20] A. Mukherjee, D. Vasileska and A.H. Goldan, *Hole transport in selenium semiconductors using density functional theory and bulk Monte Carlo*, *J. Appl. Phys* **124** (2018) 235102.

2023 JINST 18 P04021